COMPREHENSIVE STUDY OF THE EFFECT OF THE IRRADIATION TEMPERATURE ON THE BEHAVIOR OF CUBIC ZIRCONIA

A. Debelle, L. Thome, S. Moll, B. Décamps, F. Garrido, J. Channagiri, Alexandre Boulle, M. Behar, J. Jagielski

To cite this version:

A. Debelle, L. Thome, S. Moll, B. Décamps, F. Garrido, et al.. COMPREHENSIVE STUDY OF THE EFFECT OF THE IRRADIATION TEMPERATURE ON THE BEHAVIOR OF CUBIC ZIRCONIA. Journal of Applied Physics, 2014, 115 (18), pp.183504. 10.1063/1.4874795 . hal-02193729

HAL Id: hal-02193729

https://hal.science/hal-02193729v1

Submitted on 24 Jul 2019

COMPREHENSIVE STUDY OF THE EFFECT OF THE IRRADIATION TEMPERATURE ON THE BEHAVIOR OF CUBIC ZIRCONIA

A. Debelle(a*), L. Thomé(a), S. Moll(a¤), B. Décamps(a), F. Garrido(a)

(a) Centre de Sciences Nucléaires et de Sciences de la Matière, Univ. Paris-Sud, CNRS/IN2P3, 91405 Orsay, France.

J. Channagiri(b), A. Boulle(b)

(b) Science des Procédés Céramiques et Traitements de Surface, CNRS UMR 7315, Centre Européen de la Céramique, 12 rue atlantis, 87068 Limoges Cedex, France.

M. Behar(c)

(c) Instituto de Física, Universidade Federal do Rio Grande do Sul, C.P. 15051, 91501-970 Porto Alegre, RS, Brazil.

J. Jagielski(d,e)

(d) Institute for Electronic Materials Technology, Wolczynska 133, 01-919 Warsaw, Poland.

(e) The Andrzej Soltan Institute for Nuclear Studies, 05-400 Swierk/Otwock, Poland.

*Corresponding author: aurelien.debelle@u-psud.fr

¤ Present address: AREVA TN, 1 rue des Hérons, 78180 Montigny-le-Bretonneux

ABSTRACT

Cubic zirconia single-crystals (YSZ) have been irradiated with 4 MeV Au^{2+} ions in a broad fluence range (namely from 5×10^{12} to 2×10^{16} cm^{-2}) and at five temperatures: 80, 300, 573, 773 and 1073 K. Irradiated samples have been characterized by Rutherford backscattering spectroscopy in channeling mode (RBS/C), X-ray diffraction (XRD) and transmission electron microscopy (TEM) techniques in order to determine the disordering kinetics. All experimental results show that, whatever is the irradiation temperature, the damage build-up follows a multi-step process. In addition, the disorder level at high fluence is very similar for all temperatures. Thus, no enhanced dynamic annealing process is observed. On the other hand, transitions in the damage accumulation process occur earlier in fluence with increasing temperature. It is shown that temperature as low as 573 K is sufficient to accelerate the disordering process in ion-irradiated YSZ.

I - INTRODUCTION

Exposure of materials to severe irradiation coming from highly energetic particles usually appears as a detrimental process since it is generally accompanied with defect creation leading to (micro-) structural changes and eventually to materials properties degradation. This is currently a central topic in the area of nuclear energy generation where materials must face irradiation by products of fission or fusion reactions (e.g. neutrons, fission fragments, recoil nuclei). In the case of fission, one of the main issues is the safe encapsulation and management of nuclear wastes extracted during the reprocessing of spent fuel. Two options, not exclusive from each other, are currently explored: (i) immobilization (principally for long-term geological disposal) of high-level wastes in suitable solid materials named waste forms [1] and (ii) reduction of plutonium and minor actinides inventories (but not fission products) using inert-matrix fuel (IMF) [2]. IMF could also be a waste form for direct disposal after one cycle of burn-up and/or a transmutation target to decrease the radiotoxicity of minor actinides [3]. Candidate materials for these applications must satisfy a few mandatory criteria such as structural stability and efficient radionuclides confinement under irradiation (see e.g. [4]).

Cubic yttria-stabilized zirconia (YSZ) is a ceramic material with the same crystallographic structure (fluorite) than that of oxides of actinides, which makes it really suitable for incorporating Pu and minor actinides as solid solutions. Moreover, YSZ exhibits a very high radiation resistance, suggesting potential use as an IMF. This radiation resistance has been demonstrated in a series of experimental studies where the irradiation environment has been simulated with external ion beams [5-12] or also via computational approaches [13-15]. All works put forward that YSZ maintains its structural integrity up to very high irradiation levels (~100 displacements per atom, dpa). No amorphization has been detected, except when a significant concentration of particular atomic species such as Cs is introduced in the crystalline lattice [16-17], but the required Cs concentration (~8%) is well above that expected in an IMF. When YSZ is irradiated in the nuclear energy-loss regime, it exhibits a multi-step damage build-up [5,18-19], each step being characterized by a predominant type of radiation defects. For instance, in the first step, small defect clusters are preferentially formed; these clusters turn into dislocation loops in the second step and eventually a network of tangled dislocations is observed at the end of this step [10,18]. A third step also takes place at higher fluence but it depends on the nature of the irradiation particle. When no specific ion (such as Cs or noble gas) is used, a specific microstructure revealing an apparent, partial recovery of damage is observed [10]. Hence, YSZ accommodates the radiation damage by undergoing microstructural transformations that allow maintaining the long-range order; however, it has been shown that collisions cascades severely affect the short-range order [20]. Worth mentioning is that the majority of previous works on ion-irradiated YSZ have been carried out at or below room-temperature (RT) and only very few studies were devoted to the investigation of the damage produced above RT [15,21-22]. Exceptions are the works that dealt with the particular topic of gas bubble precipitation [23-24].

The present paper aims at studying the effect of the irradiation temperature on the behavior of cubic zirconia. For this purpose, YSZ crystals were irradiated with 4 MeV Au^{2+} ions in a broad fluence range (from $5x10^{12}$ to $2x10^{16}$ cm^{-2}) and from liquid nitrogen temperature (80 K) up to 1073 K. Using a combination of several experimental techniques, namely Rutherford backscattering spectroscopy and channeling (RBS/C), X-ray diffraction (XRD) and transmission electron microscopy (TEM), a detailed characterization of the irradiation damage is presented. Mobility of irradiation defects is clearly found to play a key role in the microstructural changes observed in irradiated YSZ.

II - EXPERIMENTAL

The samples used in this study are common YSZ single crystals (<100> orientation) containing 9.5 mol% Y_2O_3, synthesized by Crystal-GmbH. Prior to ion irradiations and RBS/C measurements, all samples were coated with a conductive carbon layer (thickness ~ 10 nm) to avoid charge effects.

Ion irradiations were performed at five temperatures (80K, RT, 573 K, 773 K and 1073 K) with 4 MeV $^{197}Au^{2+}$ ions. Irradiations at 80 K were conducted at the 3 MeV Tandetron of the Instituto de Fisica of the Universidade Federal of Rio Grande do Sul and irradiations from RT to 1073 K were performed at the ARAMIS accelerator of the CSNSM at Université Paris-Sud in Orsay. Irradiations were performed 7° off the normal of the surface crystals to avoid channeling phenomenon and a beam raster system was used to ensure a uniform ion irradiation; besides, in order to minimize target heating, the ion current during irradiation was maintained under 0.5 $\mu A.cm^{-2}$. The mean projected range of Au particles has been estimated, based on SRIM calculations [25], to be R_P ~ 530 nm with a range straggling ΔR_P ~ 140 nm. Ion fluences ranged from $5x10^{12}$ to $2x10^{16}$ cm^{-2}; the corresponding conversion factor for the displacements per atom (dpa) at the damage peak is ~$4.5x10^{-15}$ $dpa.cm^2$, as determined by SRIM calculations using threshold displacement energy of 40 eV for both Zr and O sublattices. Therefore, the dpa ranged from ~0.02 to ~90.

RBS/C experiments were carried out in both random and channeling (along the <100> axis) geometries by using a $^4He^{2+}$ beam of 3.12 MeV. The detector was placed at a 165° angle with respect to the beam direction. The energy resolution of the experimental setup was about 16 keV. Damage depth distributions were extracted from the analysis of RBS/C spectra with Monte-Carlo simulations performed by using the McChasy computer code [26] and assuming that a fraction of atoms (f_D) are randomly displaced from their regular crystallographic position.

XRD measurements were performed with two different apparatus that are described in [27 and references therein]. It is worth mentioning that a parallel and monochromatic (λ=0.15406 nm) incident X-ray beam was used and the 2θ angular resolution was at least of 0.01°. Symmetric θ-2θ scans and reciprocal space maps (RSMs) were recorded in the vicinity of the (400) Bragg reflection (2θ ~ 73.575°) of zirconia. θ-2θ scans were fitted with a dedicated computer-code program already presented in [28] and [29]. The formalism used in this paper is the one presented in Ref. [30]. It is worth reminding here that ($-q_N/H_{(400)}=\varepsilon_N$) represents the elastic strain in the direction normal to the surface of irradiated samples. The disorder parameter derived from the simulation of the XRD curves is the so-called static Debye-Waller (DW) factor, $exp(-L_H)$ [28-29], which varies from 1 for a perfect crystal to 0 for an amorphous-like structure; in the present work, the quantity $(1-exp(-L_H))$ is plotted for an easier comparison with the damage parameter (f_D) obtained by RBS/C.

Cross-sectional TEM samples of irradiated crystals were prepared by mechanical polishing down to electron transparency by using the wedge technique. Final polishing was done with colloidal silica commercialized by Escil. Conventional TEM observations were performed in Orsay with a FEI Tecnai G^{2}20 transmission electron microscope operated at 200 keV. To avoid charge effects during TEM observations, a ~5 nm thick carbon layer was deposited on the surface of the lamellas.

III. RESULTS

III.1. RBS/C

Figure 1 shows RBS/C spectra registered on YSZ crystals, before and after irradiation at various temperatures and ion fluences. For clarity reasons, a few selected spectra are presented only for three irradiation temperatures (80 K, 573 K and 1073 K). However, these three temperatures are representative of the whole temperature range investigated in this paper. In addition, it should be mentioned that results for RT and (partially) for 773 K have already been published in Refs [18] and [31], respectively. The spectra registered in random orientation display a plateau (below 2600 keV) and a peak (around 1000 keV) which correspond to the backscattering of analyzing particles from the Zr and O atoms of the target, respectively. Note that the O signal is enhanced due to the existence of the $^{4}He(^{16}O,^{16}O)^{4}He$ resonant reaction at 3.038 MeV. Spectra registered in channeling orientation on virgin crystals obviously exhibit a much lower yield than the random ones. Spectra registered in channeling orientation on ion-irradiated crystals show, as compared to those for virgin samples, an increase in the backscattering yield (around 2200 keV) due to the creation of a shallow damaged layer. A comparable evolution of the spectra with increasing fluence is observed for the different temperatures, *i.e.* the backscattering yield increases with fluence (up to 3-5x10^{15}) without reaching the random level. However, this apparent similarity exhibits a major difference that is readily noticed when comparing the spectra corresponding to crystals irradiated at the same fluence, namely 10^{15} cm^{-2}: rising the temperature leads to a significant increase of the backscattering yield. It should be stated that a decrease of the backscattering yield was measured for fluences higher than those presented in Figure 1 (as already clearly evidenced in [18-19]) but, since this third step is not the central point of the paper, the corresponding spectra are not displayed for the sake of clarity.

RBS/C spectra were fitted (lines in Fig. 1) with the McChasy Monte-Carlo code [26] in order to extract the damage depth distributions presented in Figure 2. The calculated data confirm the above statements. First, irrespective of the irradiation temperature, the damage profiles have a similar shape, with a thickness comprised between 1 and 1.2 µm and a peak located around 500 nm (in agreement with SRIM predictions). Second, f_D is very small (~0.1) at low ion fluence (2x10^{14} cm^{-2}) and does not exceed 0.5 at high fluence (3-5x10^{15} cm^{-2}). However, at a given fluence, for instance 10^{15} cm^{-2}, f_D equals 0.1 at 80 K, 0.3 at 573 K and 0.4 at 1073 K, suggesting that the disordering build-up is accelerated with increasing temperature.

III.2. XRD

Figure 3 displays θ-2θ scans recorded in the vicinity of the (400) reflection for YSZ crystals irradiated at various temperatures and ion fluences. Here again, it is worth mentioning that only a selection of XRD scans for three irradiation temperatures are presented but the data has been collected for the two other temperatures (RT and 773 K) as well. All XRD curves exhibit an intense narrow peak on the high-angle side that corresponds to the unirradiated part of samples. For the irradiated samples, and for all temperatures, an additional signal is observed on the low-angle side; this signal comes from the irradiated part of the crystals. This finding indicates that the irradiated region is under tensile strain in the direction normal to the surface. Moreover, the asymmetrical intensity distribution in this region indicates the existence of a dilatation gradient associated to the energy-deposition profile of Au^{2+} ions. With increasing ion fluence, the signal from the damage region first moves towards lower angles, indicating an increase of the tensile strain. Then, the fringe pattern vanishes and the scattered intensity dramatically decreases, indicating a strong increase of random atomic displacements. This change is ascribed to the re-arrangement of initial defect clusters into extended defects with a new configuration (see TEM results below and discussion) which strongly distort the crystal lattice. Note that this mechanism seems to occur at all temperatures.

Simulations of XRD data are also shown in Fig. 3 (solid lines). It can be noticed that a very good agreement is obtained between simulated and experimental data. Note that even curves corresponding to high-fluence irradiated samples are well fitted (for which no fringe pattern is recorded). This possibility was not used by authors in previous works and, as described hereafter, it has a dramatic influence on the interpretation of the XRD results. The strain and disorder profiles obtained from the simulations are shown in Figure 4. Strain profiles (Fig. 4(a),(c),(e)) show that, in agreement with the qualitative observation of the XRD curves, the maximum strain level increases with increasing fluence for all temperatures. In addition, it can also be observed that the width of the strained region increases with ion fluence. For the last fluence, at all temperatures, the strain profiles exhibit an unrealistic oscillating shape in a region around the damage peak (plotted as dotted lines in Figs. 4). This behavior can be understood by examining the disorder (*1-DW*) profiles displayed in Fig. 4(b),(d),(f). Indeed, in addition to an increase of the disorder level and to a broadening of the profile with the fluence, at the highest fluence (and for all temperatures), the disorder level appears to be very high (≥0.95) over a large thickness (~1 µm). This finding indicates that the YSZ crystals in these regions are so defective that their diffracted Bragg intensity is virtually nil, *i.e.* almost no X-rays are emitted from these regions in the symmetrical θ-2θ configuration (and for the (400) reflection). As a consequence, no physical strain value related to these regions can be obtained by XRD. This simple observation explains the occurrence of an apparently unphysical behavior of the strain in these regions. While the strain in the most defective region cannot be monitored, the strain at the damaged/pristine interface can be accurately determined. This point is addressed in more details in the discussion section and particularly with the strain build-ups.

Fig. 5 presents XRD-RSMs for YSZ crystals irradiated at the same fluence - 10^{15} cm^{-2} - but at three different temperatures. A similar comparison of RBS/C spectra pointed out an acceleration of the disordering process with temperature (see III.1.). This statement is confirmed here. The RSMs are clearly different and can be attributed, based on previous works [10,27], to different steps of the damage build-up: the map obtained for the sample irradiated at 80 K (Fig. 5(a)) is characteristic of the first step of the damage build-up, the one recorded for the crystal irradiated at 573 K (Fig. 5(b)) rather corresponds to the beginning of the second step and the last map for the crystal irradiated at 1073 K (Fig. 5(c)) matches that expected at the end of the second step.

Fig. 6 presents XRD curves recorded on YSZ crystals irradiated at RT at two fluences and the curves corresponding to these crystals after annealing (in Ar atmosphere) during 30 minutes at 1073 K. A shift of the scattered intensity towards the Bragg peak of pristine YSZ (with no broadening of this latter) is readily observed for both fluences, indicating a lattice recovery. This result was also verified by RBS/C (not shown here) and will be addressed in the discussion section.

III.3. TEM results

Figure 7 displays TEM images recorded on crystals irradiated at RT and 1073 K at different steps (as identified for RT irradiations, see [10,18]) of the damage build-up: Figs. 7((a)-(b)) reflect the first step, Figs. 7((c)-(d)) correspond to the beginning of second step and Figs. 7((e)-(f)) are characteristic of the end of the second step. Images for RT irradiation show the formation of small defect clusters in the first step of the irradiation process (Fig. 7(a)), followed by the creation of dislocation loops (Fig. (7c)) and finally a network of tangled dislocations is observed (Fig. (7e)). A more complete description of these microstructural changes is addressed hereafter. Identical defects and microstructures are observed for irradiation at 1073 K, as clearly evidenced in Fig. 7(b), (d), (f) that correspond to the first step, the beginning and end of the second step, respectively. It can thus be reasonably assumed that these results also hold for the intermediate temperatures. An analogous microstructural evolution has been reported in recent works in other fluorite-type structured ceramic oxides irradiated in similar conditions, such as in CeO_2 irradiated with 500 keV Xe at 800°C [40] and in UO_2 irradiated with 150 keV Kr at 600°C and with 1 MeV Kr at 800°C [41].

IV. Discussion

Change in the irradiation temperature may affect the damage creation and recovery rates, as readily demonstrated in strontium titanate (STO) [32], silicon carbide (SiC) [33-34] and some pyrochlores [35]. These materials exhibit very low damage level when irradiated above a threshold temperature whereas they otherwise undergo amorphization. The radiation behavior of ion-irradiated solids is generally assessed by determining the damage accumulation build-up, which is the variation of a given disorder parameter with the ion fluence. Figure 8 presents the evolution of the damage level obtained by RBS/C; experimental data are fitted with the multi-step damage accumulation model (MSDA) [36-37] already used to account for former experimental results obtained on e.g. ion-irradiated zirconia [16], SiC [38] and pyrochlores [39]. Briefly, this model assumes that the damage accumulation process occurs in several (*n*) distinct steps, each step being triggered by the destabilization of the current structure of the material, and the successive structural transformations are described by a direct impact mechanism. Fits to RBS/C data with this model are represented by solid lines in Fig. 8. Three steps (n=3) are required to interpret results obtained for all irradiation temperatures (note that irradiation at very high fluence was not performed at 573 K). In addition, except at 80 K where surprisingly the maximum damage at the end of the second step is found to be lower than that at RT, the overall damage level is slightly decreased with increasing temperature over such a large temperature range. In other words, no temperature-enhanced dynamic annealing is observed in YSZ and a same multi-step disordering process occurs in this material whatever is the irradiation temperature.

Beyond this similar overall behavior with irradiation temperature, a major difference emerges from the comparison of the damage build-ups in YSZ. Actually, there is a significant variation of the threshold fluence for the onset of the second damage step when the irradiation temperature is varied (except between 80 K and 300 K where no shift is observed). Values of fluences for the onset of step 2 are listed in Table I. For instance, this fluence is found to be

~1.2×10^{15} cm^{-2} for irradiation at 80 K and ~0.15×10^{15} cm^{-2} at 1073 K. In other words, the higher the irradiation temperature, the earlier is the transition between step 1 and step 2.

Disordering build-ups derived from XRD data, *i.e.* the variation of the disorder parameter *(1-DW)* and of the strain level (ε_N) as a function of ion fluence, were also determined for all temperatures (Figs. 9(a-b)). A two-step process (the third one is not accessible by XRD) is observed concerning the disorder parameter (Fig. 9(a)) for the five investigated temperatures. Besides, fluences (graphically determined) for the onset of the second step are very similar to those obtained from RBS/C measurements (see Table I). An equal apparent 100% disorder level is reached at high fluence for all temperatures, indicating that, from the XRD technique, crystals at this stage appear severely defective (with a most likely identical microstructure). Conversely, in the first irradiation step, different disorder levels are observed, values being lowered when the irradiation temperature is increased. This result could be related to a decrease of the defect density with increasing temperature. The strain build-ups presented in Fig. 9b look different from those previously reported by the authors [18,27] or by another group also working on irradiated YSZ [19]. In particular, as previously explained in [29] and mentioned in section III.2., a two-step process is still observed but no strain relaxation is reported in the second step. This difference can be explained by the fact that the strain is no longer determined by a simple observation of the XRD data, but derived from the simulation of the whole experimental curves. Apart from the Bragg peak due to the unperturbed crystal, the curves obtained on irradiated crystals at high fluences display broad pseudo-peaks originating from heavily damaged regions ($1 - DW \sim 1$) whose position is not related to the actual level of strain in the irradiated region. The simulations show that the strain keeps on increasing at high fluence in the regions surrounding the damage peak (see Fig. 4(a)-(c)). For this reason, the strain actually continues to increase in the second step of the damage build-up. This result holds for the whole temperature range. The five strain build-ups presented in Fig. 9(b) can be separated into two groups: 80 K and RT on the one hand and 573 K, 773 K and 1073 K on the other hand. For the former group (at low temperature), strain levels are high with values ~0.4% in the first step and ~0.9% in the second step. For the latter group (high temperature), strain levels are much lower with values ranging from ~0.1% to ~0.5%. This difference in the strain level as a function of the irradiation temperature appears very similar to that recently reported by Yang. *et al.* who monitored the strain in YSZ irradiated with ions of different velocities [19]. They found that the strain level in the first step decreased with increasing velocity, an effect which was tentatively attributed to an ionization-induced enhanced defect-mobility due to a larger electronic energy loss. This interpretation could hold for the present results, with thermal energy playing the role of electronic energy. At low temperature, transition from the first step to the second one takes place at ~10^{15} cm^{-2} while at high temperature it occurs at ~5×10^{14} cm^{-2}. There is no progressive shift as observed for the damage (RBS/C) and disorder (XRD) kinetics because the strain is not monitored at the same depth as a function of the ion fluence. These results indicate that the strain relaxation is not the (main) driving force for the formation of the dislocation loops, *i.e.* for the occurrence of the second step of the damage build-up.

The first transition of the damage accumulation process is shown to associated to the transformation of black dots into black/black lobes that eventually form dislocation lines (see TEM images in Fig. 7). Yasuda et al. [22] studied this microstructure change mechanism and concluded, based on earlier works from Baufeld *et al.* [42], that defects created in the first stage of the irradiation process are seeds for dislocation loops. More precisely, the following mechanism was proposed [22,42]: (i) interstitial point defect agglomerate and (ii) form Frank loops with Burgers vectors $b = {}^{a}\!/_{3} < 111 >$ (i.e. dislocations bounding a stacking fault); (iii) these loops grow and transform into perfect (unfaulted) dislocation loops via the spontaneous nucleation of a Shockley partial dislocation according to the following equation ${}^{a}\!/_{6} < 11\bar{2} > + {}^{a}\!/_{3} < 111 > \rightarrow {}^{a}\!/_{2} < 110 >$; (iv) finally, growth of these perfect loops leads to the formation of a network of dislocation lines. It is worth mentioning that the mechanism for the transformation of partial into perfect dislocation loops has also been reported in irradiated ceria (see [43] and references therein). Both Baufeld et al. [42] and Yasuda et al. [22] postulated the existence of a critical defect size above which the actual defect is not stable anymore and turn into a new, stable one. This assumption has been supported by a theoretical model developed by Ryazanov *et al.* [44] taking into account the charge state of the dislocation loops to explain their instability (hence their transformation into dislocation lines) above a critical size. The critical size was found to be on the order of a micrometer when the defect density is low and smaller when the loop density increases (*i.e*. when the mean distance between loops decreases). Such a hypothesis of a critical size could perfectly explain the difference in the threshold fluence for the onset of step 2 observed in YSZ in the present work. Indeed, the shift of the transition fluence to lower values with increasing temperature would mean that the critical size is reached more rapidly. This is possible by assuming that increasing the temperature induces a higher defect mobility leading to an enhanced defect-clustering process. In addition, such an increased defect-clustering rate could also account for the decrease of the defect density explaining why (XRD) disorder and strain levels decrease with temperature. It is worth noting that this effect is already operational at 573 K, a temperature which seems rather low but is consistent with experimental observations of Baufeld *et al.* of an accelerated defect growth above 473 K [42]. This result confirms the high mobility of the irradiation point defects in YSZ.

Finally, it is worthwhile to highlight that the thermally-assisted defect clustering process only occurs upon irradiation. Indeed, after a thermal annealing at 1073 K during 30 minutes, YSZ crystals irradiated at RT in the first step (10^{15} cm^{-2}) and at the end of the second step ($5x10^{15}$ cm^{-2}) of the damage build-up exhibit a significant damage recovery. This finding is illustrated for instance in Fig. 6 that presents XRD curves recorded on as-irradiated and post-annealed YSZ samples. In other words, post-irradiation thermal energy does not drive the structure towards a more defective one (towards the right side of the damage kinetics) but towards a less defective one, unlike thermal energy brought during irradiation. This difference of behavior between temperature effects during irradiation *vs.* after irradiation can be ascribed to static vs. dynamic processes (for instance defect migration) and to equilibrium *vs*. out-of-equilibrium conditions. More generally, differences in the effects of ion irradiation *vs*. thermal annealing have already been pointed out in several cases, such as for atomic mixing (for which heat of formation are modified under irradiation, see e.g. [45-46]), formation of nanostructures [47] and stress relaxation in sputtered thin films [48].

IV - CONCLUSION

Cubic zirconia single-crystals have been irradiated with 4 MeV Au^{2+} ions in broad fluence (from $5x10^{12}$ to $2x10^{16}$ cm^{-2}) and temperature (from 80 to 1073 K) ranges. Crystals have been characterized by RBS/C, XRD and TEM in order to get a comprehensive understanding of the behavior of this ceramic under ion irradiation.

Results show that whatever is the irradiation temperature, the damage build-up obeys a multi-step process (contrary to what is observed in other materials such as SiC or STO). Each step is characterized by specific disorder and strain levels corresponding to a well-defined microstructure. In the first step, small clusters of point defects are formed which are seeds for Frank dislocation loops that transform into perfect dislocation loops in the second step. At the end of this second step, a network of dislocation lines is observed, and in the third step dislocations reorganize to form dislocation walls. Dynamic (*i.e.* inside collision cascades) annealing is very efficient in YSZ but this self-healing process is definitely not enhanced with increasing irradiation temperature; in fact, only a slight decrease in the final disorder level is observed over the broad temperature range. On the other hand, an increase of the irradiation temperature provides a larger mobility to radiation defects which presumably leads to an enhanced defect clustering. This mechanism triggers the observed microstructural transformations through the existence of a critical size above which the defect nature changes. Consequently, transitions in the damage accumulation process occur earlier in fluence with increasing temperature. It is worth mentioning that temperature as low as 573 K is sufficient to accelerate the disordering process in irradiated YSZ.

These basic results should be taken into account when considering YSZ as an IMF since temperatures higher than 573 K will be reached in fast neutron reactors.

Acknowledgments

A.D., B.D., L.T. and F.G. would like to acknowledge the SEMIRAMIS staff for carrying out ion irradiations at high temperature. XRD measurements on the Panalytical diffractometer have been performed at the nanocenter CTU-IEF-Minerve that is partially funded by the “Conseil Général de l’Essonne”. This work was partially funded by the NEEDS-Matériaux program. J.C. is grateful to Région Limousin for partial funding of this study.

REFERENCES

[1] W. Lutze, R. C. Ewing, Radioactive Waste Forms for the Future, North-Holland, 1988.

[2] C. Degueldre, J.M. Paratte, J. Nucl. Mater. 274 (1999) 1.

[3] R. J. M Konings, K. Bakker, J.G. Boshoven, H. Hein, M.E. Huntelaar, R.R. van der Laan, J. Nucl. Mater. 274 (1999) 84.

[4] W. J. Weber, R. C. Ewing, C. R. A. Catlow, T. Diaz de la Rubia, L. W. Hobbs, C. Kinoshita, Hj. Matzke, A. T. Motta, M. Nastasi, E. K. H. Salje, E. R. Vance and S. J. Zinkle, J. Mater. Res. 13 (1998) 1434.

[5] K.E. Sickafus, Hj. Matzke, Th. Hartmann, K. Yasuda, J.A. Valdez, P. Chodak III, M. Nastasi, R.A. Verall, J. Nucl. Mater. 274 (1999) 66.

[6] L.M. Wang, S.X. Wang, R.C. Ewing, Phil. Mag. Lett. 80 (2000) 341.

[7] G. Sattonnay, M. Lahrichi, M. Herbst-Ghysel, F. Garrido, L. Thomé, J. Appl. Phys. 101 (2007) 103516.

[8] J.-M. Costantini, F. Guillet, S. Lambert, D. Grébille, F. Beuneu, Ch. Trautmann, J. Appl. Phys. 104 (2008) 073504.

[9] J.-M. Costantini, F. Beuneu, W. J. Weber, J. Nucl. Mater. 440, (2013) 508.

[10] A. Debelle, S. Moll, B. Décamps, A. Declémy, L. Thomé, G. Sattonnay, F. Garrido, I. Jozwik, J. Jagielski, Scripta Mater. 63 (2010) 665.

[11] Y. Zhang, W. Jiang, Ch. Wang, F. Namavar, Ph. D. Edmondson, Z. Zhu, F. Gao, J. Lian, W. J. Weber, Phys. Rev. B 82 (2010) 184105.

[12] X. Ou, R. Kögler, H.-B. Zhou, W. Anwand, J. Grenzer, R. Hübner, M. Voelskow, M. Butterling, Sh. Zhou, W. Skorupa, Phys. Rev. B 86 (2012) 224103.

[13] R. Devanathan, W. J. Weber, J. Mater. Res. 23 (2008) 593.

[14] R. Devanathan, Nucl. Instrum. Meth. B 267 (2009) 3017.

[15] K. Trachenko, J. M. Pruneda, E. Artacho, M. T. Dove, Phys. Rev. B 71 (2005) 184104.

[16] M. Wang, S. X. Wang, R. C. Ewing, Phil. Mag. Lett. 80 (2000) 341.

[17] L. Vincent, L. Thomé, F. Garrido, O. Kaitasov, F. Houdelier, J. Appl. Phys. 104 (2008) 114904.

[18] S. Moll, L. Thomé, G. Sattonnay, A. Debelle, F. Garrido, L. Vincent, J. Jagielski, J. Appl. Phys. 106 (2009) 073509.

[19] T. Yang, C. A. Taylor, Sh. Kong, Ch. Wang, Y. Zhang, X. Huang, J. Xue, Sha Yana, Y. Wang, J. Nucl. Mater. 443 (2013) 40.

[20] E. Zarkadoula, R. Devanathan, W. J. Weber, M. Seaton, I. T. Todorov, K. Nordlund, M. T. Dove, K. Trachenko, J. Appl. Phys. 115 (2014) 083507.

[21] K. E. Sickafus, H. Matzke, K. Yasuda, I.I.I. P. Chodak, R. A. Verrall, P. G. Lucuta, H. R. Andrews, A. Turos, R. Fromknecht, N.P. Baker, Nucl. Instr. Meth. B 141 (1998) 358.

[22] K. Yasuda, C. Kinoshita, S. Matsumura, A.I. Ryazanov, J. Nucl. Mater. 319 (2003) 74.

[23] T. Hojo, J. Aihara, K. Hojou, S. Furuno, H. Yamamoto, N. Nitani, T. Yamashita, K. Minato, T. Sakuma, J. Nucl. Mater. 319 (2003) 81.

[24] T. Hojo, H. Yamamoto, J. Aihara, S. Furuno, K. Sawa, T. Sakuma, K. Hojou, Nucl. Instr. Meth. B 241 (2005) 536.

[25] J.F. Ziegler, J. P. Biersack, U. Littmark, The Stopping and Range of Ions in Solids, Pergamon, New York, 1985. Available at: www.srim.org.

[26] L. Nowicki, A. Turos, R. Ratajczak, A. Stonert, F. Garrido, Nucl. Instr. Meth. B 240 (2005) 277.

[27] A. Debelle, L. Qasim, P. Rosza, S. Moll, A. Boulle, L. Thomé, Nucl. Instr. Meth. 277 (2011) 14.

[28] A. Boulle, A. Debelle, J. Appl. Cryst. 43 (2010) 1046.

[29] J. Channagiri, A. Boulle, A. Debelle, Nucl. Instr. Meth. B, in press.

[30] A. Debelle, A. Declémy, Nucl. Instr. Meth. B 268 (2010) 1460.

[31] S. Moll, A. Debelle, L. Thomé, G. Sattonnay, J. Jagielski, F. Garrido, Nucl. Instr. Meth. B 286 (2012) 169.

[32] Y. Li, R.J. Liu, W-K. Chu, T.J. Tate, Phys. Rev. B 57 (1998) 5668.

[33] W. J. Weber, L. Wang, Y. Zhang, W. Jiang, I.-T. Bae, Nucl. Instrum. Meth. B 266 (2008) 2793.

[34] E. Wendler, Th. Bierschenk, W. Wesch, E. Friedland, J. B. Malherbe: Nucl. Instrum. Meth. B 268 (2010) 2996.

[35] G. R. Lumpkin, K. R. Whittle, S. Rios, K. L. Smith, N. J. Zaluzec, J. Phys.: Condens. Matter 16 (2004) 8557.

[36] J. Jagielski, L. Thomé, Appl. Phys. A 97, (2009) 147.

[37] J. Jagielski, L. Thomé, Rad. Eff. & Def. Solids, 166 (2011) 367.

[38] J.-F. Barbot, A. Declémy, M.-F. Beaufort, Phys. Status Solidi 210 (2013) 218.

[39] S. Moll, G. Sattonnay, L. Thomé, J. Jagielski, C. Decorse, P. Simon, I. Monnet, W. J. Weber, Phys. Rev. B 84 (2011) 064115.

[40] B Ye, A. Oaks, M. A. Kirk, D. Yun, W.-Y. Chen, B. Holtzman, J. F. Stubbins, J. Nucl. Mater. 441 (2013) 525.

[41] L.-F. He, M. Gupta, C. A. Yablinsky, J. Gan, M. A. Kirk, X.-M. Bai, J. Pakarinen, T. R. Allen, J. Nucl. Mater. 443 (2013) 71.

[42] B. Baufeld, D. Baither, U. Messerschmidt, M. Bartsch, I. Merkel, J. Am. Ceram. Soc. 76 (1993) 3163.

[43] Y. Miao, D. Aidhy, W.-Y Chen, K. Mo, A. Oaks, D. Wolf, J. F. Stubbins, J. Nucl. Mater. 445 (2014) 209.

[44] A. I. Ryazanov, K. Yasuda, C. Kinoshita, A. V. Klaptsov, J. Nucl. Mater. 307-311 (2002) 918.

[45] M. Nastasi, S. Fayeulle, Y.-C. Lu, H. Kung, Mater. Sc. Eng. A253 (1998) 202.

[46] F. Martin, C. Jaouen, J. Pacaud, G. Abadias, Ph. Djemia, F. Ganot, Phys. Rev. B 71 (2005) 045422.

[47] A. Meldrum, L.A. Boatner, C.W. White, R.C. Ewing, Mater. Res. Innovat. 3 (2000) 190.

[48] A. Debelle, A. Michel, G. Abadias, C. Jaouen, J. Vac. Sci. Technol A 25 (2007) 1438.

Table I: Threshold fluences (in cm^{-2}) for the onset of the second step of the damage build-up in ion irradiated YSZ crystals. Values obtained from RBS/C measurements derive from the fitting of experimental data with the MSDA model [36-37] and values from the XRD technique were graphically determined.

	80 K	300 K	573 K	773 K	1073 K
RBS/C	1.2×10^{15}	1.2×10^{15}	0.55×10^{15}	0.45×10^{15}	0.15×10^{15}
XRD	1×10^{15}	1×10^{15}	0.5×10^{15}	0.5×10^{15}	0.2×10^{15}

FIGURE CAPTIONS

Figure 1: RBS spectra recorded in random (stars) and <100>-axial (open symbols) directions on YSZ crystals irradiated with 4 MeV Au^{2+} ions at indicated fluences (cm^{-2}) at 80 K (a), 573 K (b) and 1073 K (c). Analyzing particles are 3.07 MeV $^4He^{2+}$ ions. Lines are simulations of RBS/C data with the Monte-Carlo McChasy code [26].

Figure 2: Damage depth distributions corresponding to simulations of RBS/C spectra presented in figure 1.

Figure 3: θ-2θ experimental scans (dots) recorded in the vicinity of the (400) reflection for virgin and irradiated YSZ crystals with 4 MeV Au^{2+} ions at indicated fluences at 80 K (a), 573 K (b) and 1073 K (c). Solid (red) lines are best fits with the dedicated simulation program [28-29]. Labels correspond to the ion fluences (expressed in cm^{-2}). Curves are shifted vertically for visualization purposes.

Figure 4: Strain ((a),(c),(e)) and disorder ((b),(d),(f)) depth distributions corresponding to simulation of XRD curves presented in figure 3.

Figure 5: Reciprocal space maps recorded in the vicinity of the (400) Bragg reflection for YSZ crystals irradiated with 4 MeV Au^{2+} ions at 10^{15} cm^{-2} and at 80 K (a), 573 K (b) and 1073 K (c).

Figure 6: θ-2θ scans recorded in the vicinity of the (400) reflection for virgin an irradiated YSZ crystals (lines) with 4 MeV Au^{2+} ions at RT at indicated fluences. Scans recorded on post-annealed (30 min. at 1073 K) samples are also displayed (symbols). Curves are shifted vertically for visualization purposes.

Figure 7: TEM bright-field micrographs recorded on YSZ crystals irradiated with 4 MeV Au^{2+} ions at 300 K (top) and 1073 K (bottom) and at different places of the damage build-up plotted in Fig. 8: (a)-(b) correspond to the first step, (c)-(d) are characteristic of the beginning of the second step and (e)-(f) illustrate microstructure observed at the end of the second step. Images were taken in the following conditions: (c) **g** = $\bar{2}\bar{2}0$, $(\bar{1}12)$ plane; (d) **g** = $2\bar{2}0$, (001) plane; (e) **g** = 111, $(\bar{1}01)$ plane; (f) **g** = 220, (001) plane.

Figure 8: Disordering kinetics (*i.e.* f_D *vs* ion fluence) derived from RBS/C data obtained for YSZ crystals irradiated with 4 MeV Au^{2+} ions at the indicated temperatures. Solid lines are fits to data using the MSDA model [36-37].

Figure 9: Disorder (*1-DW*) (a) and strain (b) kinetics derived from XRD data obtained for YSZ crystals irradiated with 4 MeV Au^{2+} ions at the indicated temperatures. Solid lines are drawn for visualization purposes.

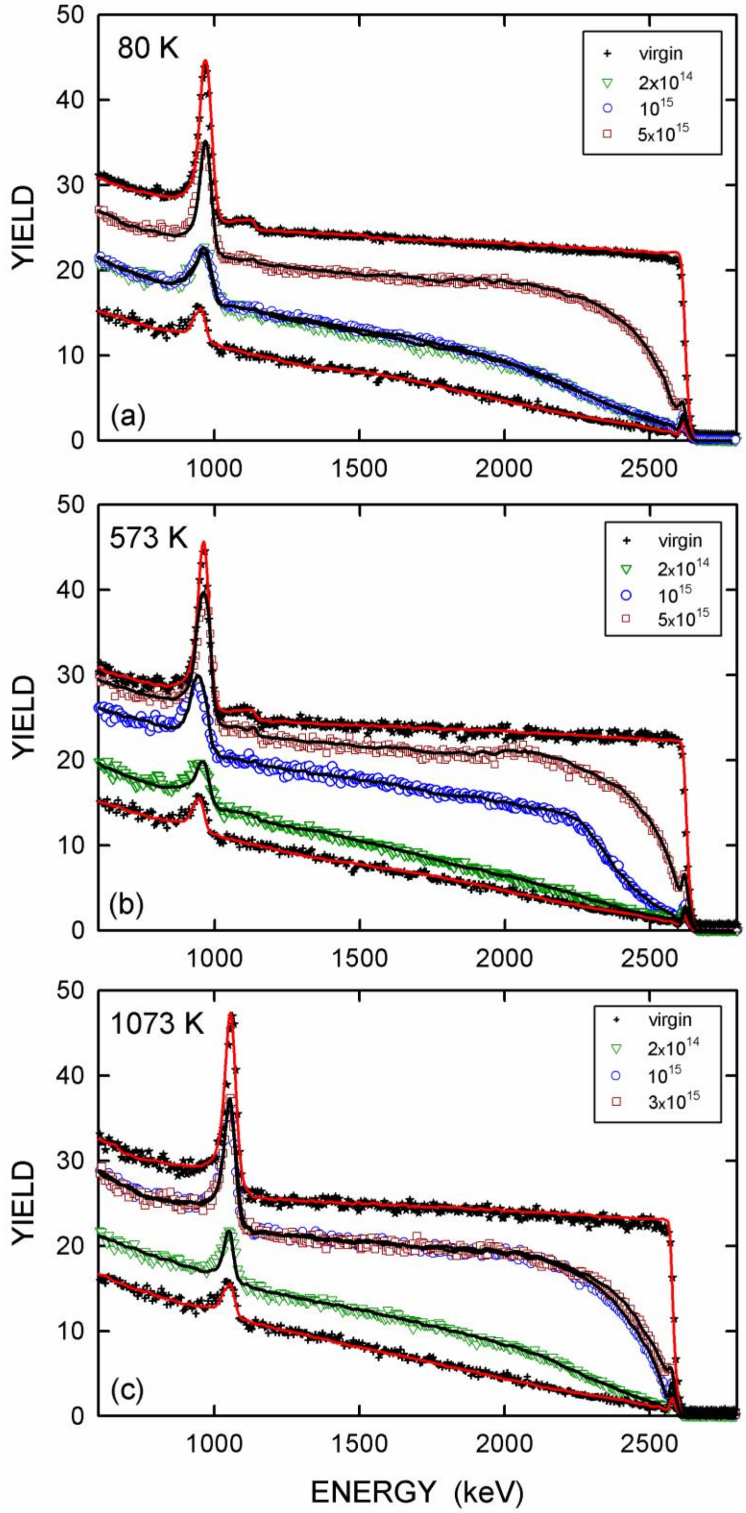
80 K
virgin
2x10^14
10^15
5x10^15
(a)
573 K
virgin
2x10^14
10^15
5x10^15
(b)
1073 K
virgin
2x10^14
10^15
3x10^15
(c)
YIELD
0
10
20
30
40
50
1000
1500
2000
2500
ENERGY (keV)

Figure 1

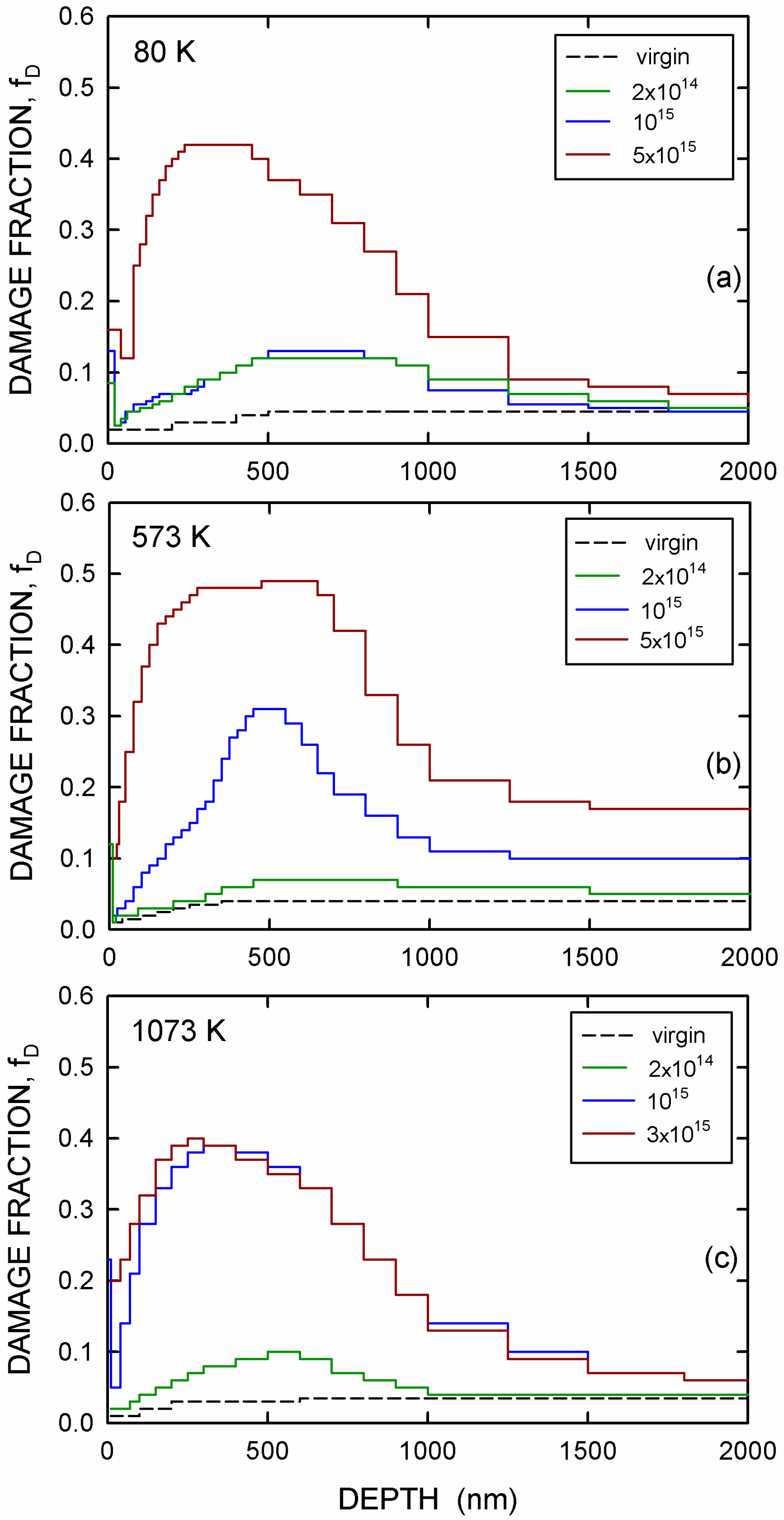

DAMAGE FRACTION, f_D
80 K
573 K
1073 K
virgin
$2x10^{14}$
10^{15}
$5x10^{15}$
$3x10^{15}$
(a)
(b)
(c)
0.0
0.1
0.2
0.3
0.4
0.5
0.6
0
500
1000
1500
2000
DEPTH (nm)

Figure 2

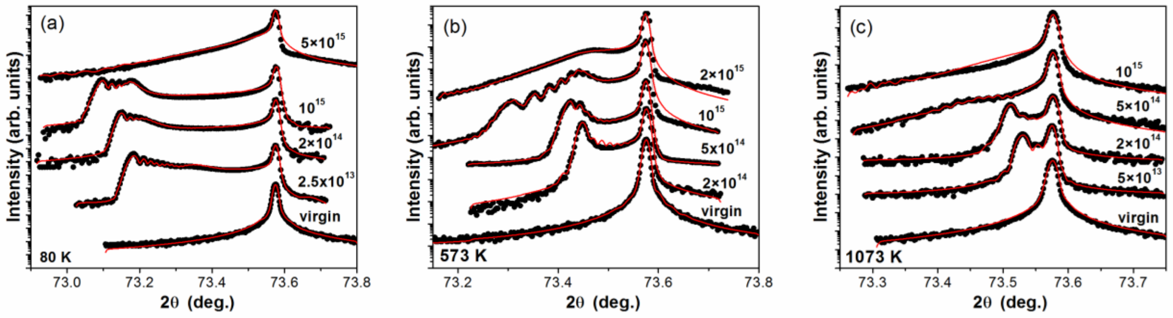
(a)
5×10^15
10^15
2×10^14
2.5x10^13
virgin
80 K
Intensity (arb. units)
73.0
73.2
73.4
73.6
73.8
2θ (deg.)
(b)
2×10^15
10^15
5x10^14
2×10^14
virgin
573 K
Intensity (arb. units)
73.2
73.4
73.6
73.8
2θ (deg.)
(c)
10^15
5×10^14
2×10^14
5×10^13
virgin
1073 K
Intensity (arb. units)
73.3
73.4
73.5
73.6
73.7
2θ (deg.)

Figure 3

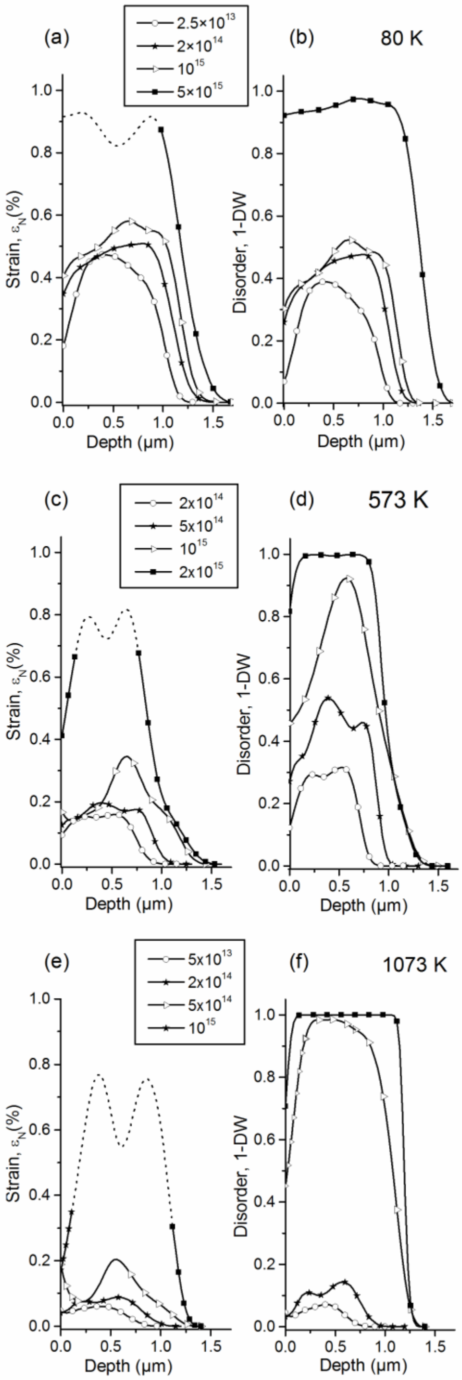
(a)
2.5×10^13
2×10^14
10^15
5×10^15
(b)
80 K
Strain, ε_N (%)
Disorder, 1-DW
Depth (µm)
0.0
0.2
0.4
0.6
0.8
1.0
0.5
1.5
(c)
2x10^14
5x10^14
10^15
2x10^15
(d)
573 K
Strain, ε_N (%)
Disorder, 1-DW
Depth (µm)
(e)
5x10^13
2x10^14
5x10^14
10^15
(f)
1073 K
Strain, ε_N (%)
Disorder, 1-DW
Depth (µm)

Figure 4

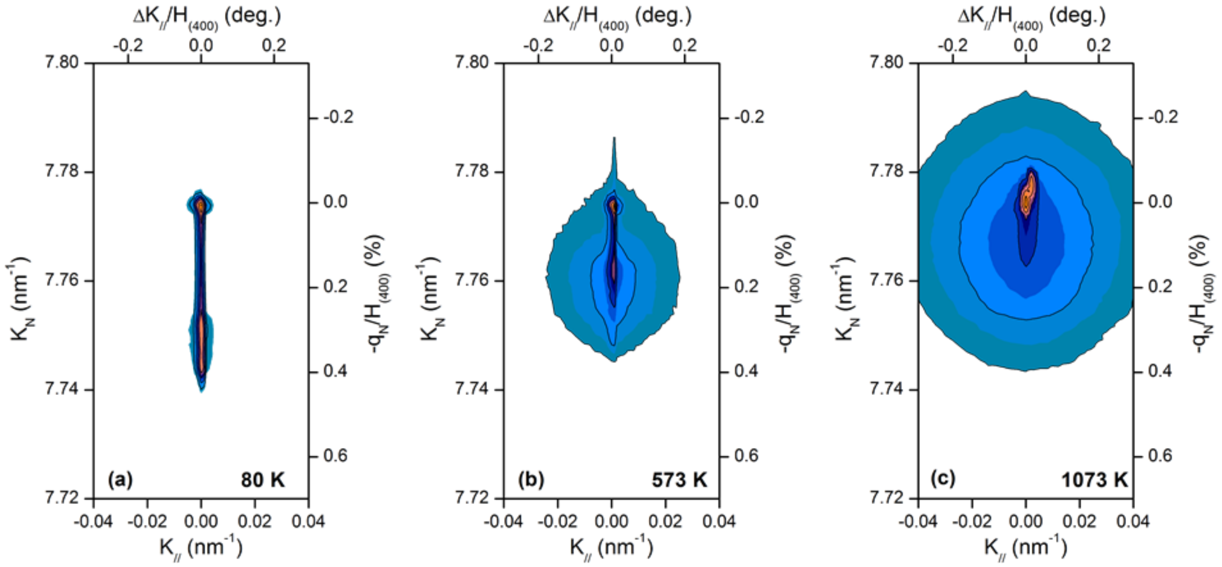
ΔK//H(400) (deg.)
-0.2
0.0
0.2
7.80
7.78
7.76
7.74
7.72
K_N (nm-1)
-0.2
0.0
0.2
0.4
0.6
-q_N/H(400) (%)
-0.04
-0.02
0.00
0.02
0.04
K// (nm-1)
(a)
80 K
(b)
573 K
(c)
1073 K

FIGURE 5

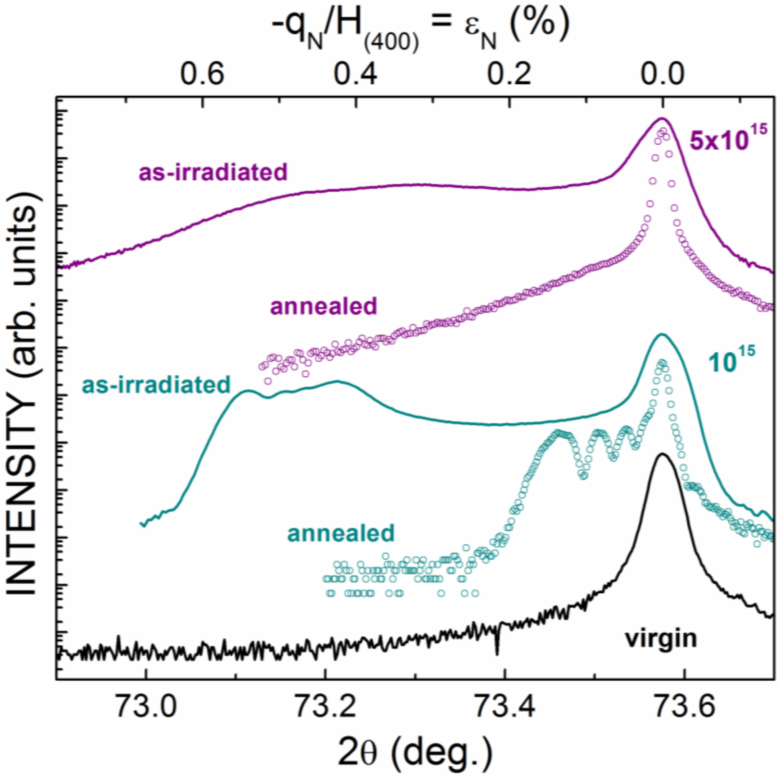
$-q_N/H_{(400)} = \varepsilon_N$ (%)
0.6
0.4
0.2
0.0
as-irradiated
5×10^{15}
annealed
as-irradiated
10^{15}
annealed
virgin
INTENSITY (arb. units)
73.0
73.2
73.4
73.6
2θ (deg.)

FIGURE 6

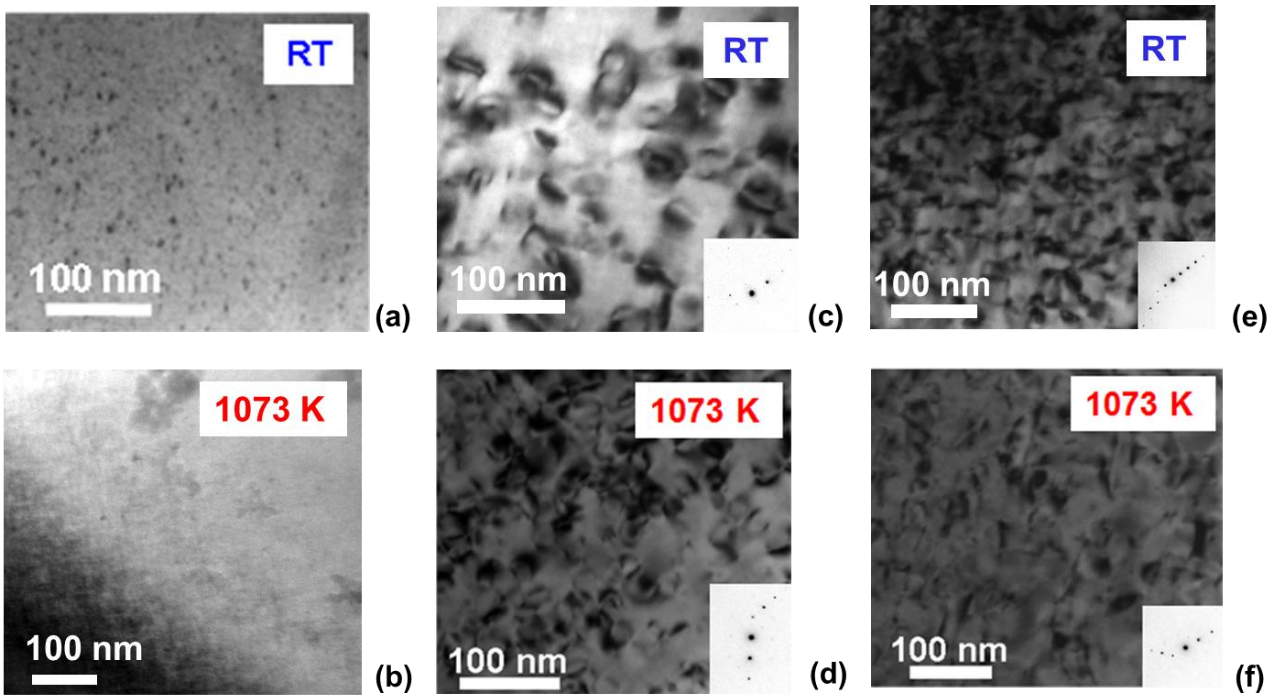
RT
100 nm
(a)
RT
100 nm
(c)
RT
100 nm
(e)
1073 K
100 nm
(b)
1073 K
100 nm
(d)
1073 K
100 nm
(f)

Figure 7

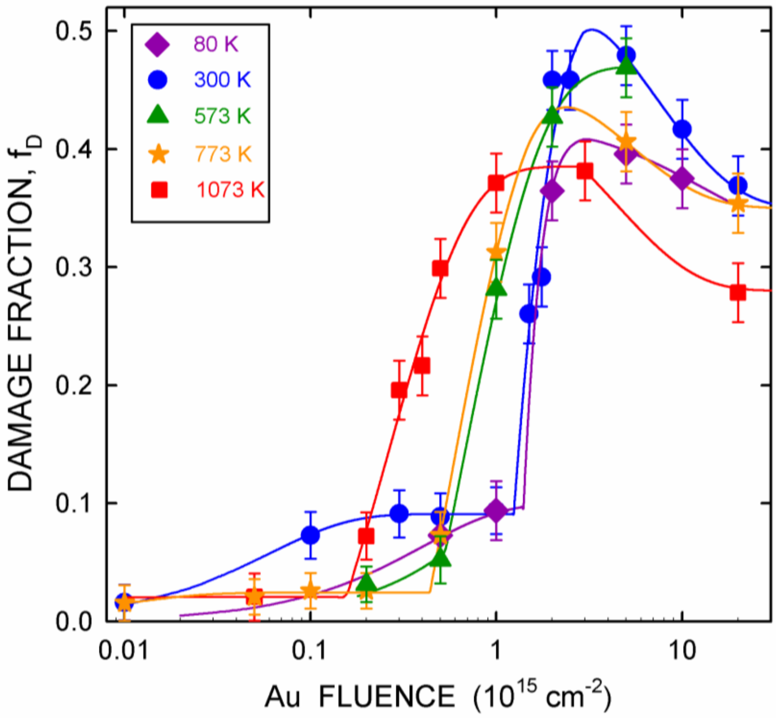
80 K
300 K
573 K
773 K
1073 K
DAMAGE FRACTION, f_D
0.0
0.1
0.2
0.3
0.4
0.5
0.01
0.1
1
10
Au FLUENCE (10^{15} cm^{-2})

Figure 8

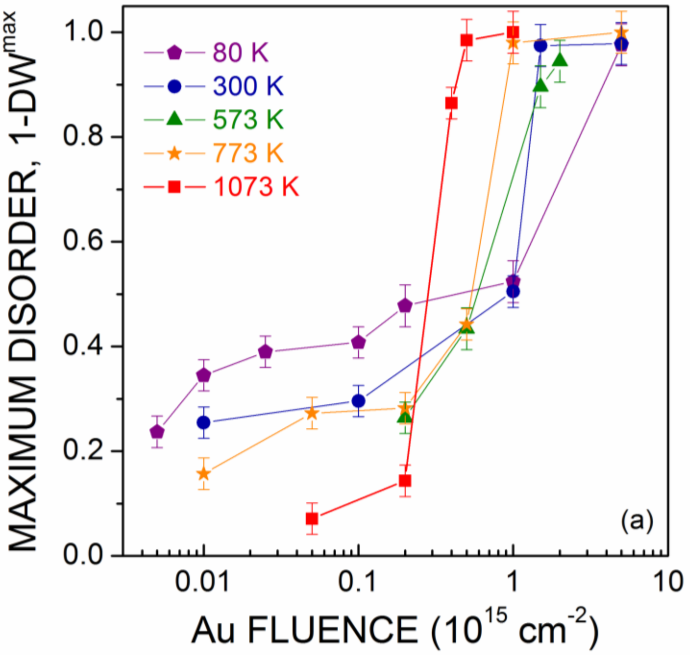

FIGURE 9(a)

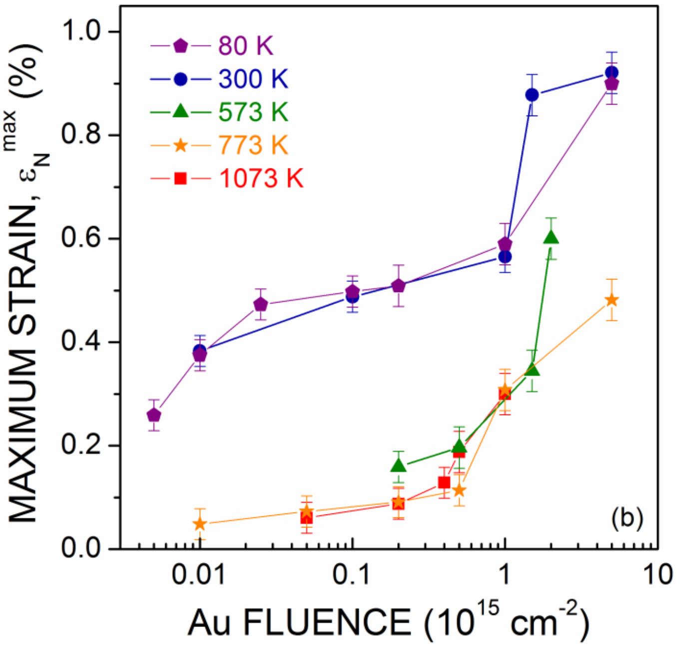

FIGURE 9(b)